

The Korea Microlensing Telescope Network (KMTNet) Alert Algorithm and Alert System

HYOUN-WOO KIM¹, KYU-HA HWANG¹, YOSHI SHVARTZVALD², JENNIFER C. YEE³,
MICHAEL D. ALBROW⁴, SANG-MOK CHA^{1,5}, SUN-JU CHUNG^{1,6}, ANDREW GOULD^{1,7,8},
CHEONGHO HAN⁹, YOUN KIL JUNG¹, DONG-JIN KIM¹, SEUNG-LEE KIM^{1,6},
CHUNG-UK LEE^{1,6}, DONG-JOO LEE¹, YONGSEOK LEE^{1,5}, BYEONG-GON PARK^{1,6},
RICHARD W. POGGE⁸ YOON-HYUN RYU¹, IN-GU SHIN³, WEICHENG ZANG¹⁰,

¹*Korea Astronomy and Space Science Institute, Daejeon 34055, Republic of Korea*

²*IPAC, Mail Code 100-22, Caltech, 1200 E. California Blvd., Pasadena, CA 91125, USA*

³*Harvard-Smithsonian Center for Astrophysics, 60 Garden St., Cambridge, MA 02138,
USA*

⁴*University of Canterbury, Department of Physics and Astronomy, Private Bag 4800,
Christchurch 8020, New Zealand*

⁵*School of Space Research, Kyung Hee University, Yongin, Gyeonggi 17104, Republic of
Korea*

⁶*Korea University of Science and Technology, 217 Gajeong-ro, Yuseong-gu, Daejeon 34113,
Republic of Korea*

⁷*Max-Planck-Institute for Astronomy, Königstuhl 17, 69117 Heidelberg, Germany*

⁸*Department of Astronomy, Ohio State University, 140 W. 18th Ave., Columbus, OH
43210, USA*

⁹*Department of Physics, Chungbuk National University, Cheongju 28644, Republic of Korea*

¹⁰*Physics Department and Tsinghua Centre for Astrophysics, Tsinghua University, Beijing
100084, China*

ABSTRACT

We describe a new microlensing-event alert algorithm that is tailored to the Korea Microlensing Telescope Network (KMTNet) multi-observatory system. The algorithm focuses on detecting “rising” events, i.e., events whose brightness is increasing as a function of time. The algorithm proceeds in three steps. It first identifies light curves with at least N_{high} points that are at least 3σ above

the median and that had been taken since shortly before the previous search for new events. It then demands that there are at least N_{high} *consecutive* high points when considering any combination of light curves from one, two, or three observatories. Finally, it fits to a “rising microlensing model” consisting of a broken line, i.e., flat before some time t_{rise} and rising linearly afterward. If this fit is better than a flat line by $\Delta\chi^2 > \Delta\chi^2_{\text{thresh}}$, the light curve is sent for human review. Here, $(N_{\text{high}}, \Delta\chi^2_{\text{thresh}}) = (5, 250)$ or $(10, 400)$, depending on the field cadence. For 2018, KMTNet alerts will initially be restricted to a few northern bulge fields and may gradually extend to the full northern bulge. Further expansion of coverage is expected in 2019.

Subject headings: gravitational lensing: micro

1. Introduction

Real-time microlensing alerts have played a crucial role in the development of the field. Prior to the discovery of the first microlensing event, Gould & Loeb (1992) had already proposed real-time alerts as a means to bridge the gap between the technical requirements of finding microlensing events and those of monitoring these events with sufficient cadence to identify and characterize planetary signatures. Even toward the densest star fields of the Galactic bulge, the microlensing event rate is only $\gamma \sim 10^{-5} \text{ yr}^{-1}$. Hence, one must monitor tens of square degrees, with typical stellar surface densities of $\sim 5 \times 10^6 \text{ deg}^{-2}$ (to limiting depth $I \lesssim 20$) to find of order 10^3 microlensing events per year. With the camera fields of view available (or foreseen) at that time, this required tiling the target area once or at most a few times per night. These low cadences $\Gamma \sim 1 \text{ day}^{-1}$ were quite adequate to find microlensing events, with their characteristic timescales $t_E \sim 20 \text{ day}$, because they still yielded $N = \Gamma t_E \sim 20$ epochs per Einstein crossing time. However, this cadence is inadequate to characterize all but the largest planets because the timescales of the planetary deviations are typically shorter than the events by $t_{\text{pert}} \sim \sqrt{q} t_E$, where q is the planet/host mass ratio. Hence, to obtain, say, five epochs per perturbation timescale (i.e., 10 over the whole perturbation) requires a higher cadence by a factor $q^{-1/2}/4$. This corresponds $\Gamma \sim (0.4, 1, 4) \text{ hr}^{-1}$ for (Saturn, Neptune, Earth) mass planets (assuming that the typical $t_E \sim 20 \text{ day}$ timescale corresponds to an $M \sim 0.5 M_{\odot}$ host). Hence, Gould & Loeb (1992) advocated intensive follow-up observations from multiple sites of individual microlensing events, which of course required that these events be identified and publicly announced while they were still ongoing and therefore sensitive to planets.

Such real-time alert systems were quickly established by the MACHO (Alcock et al.

1994) and OGLE (Udalski et al. 1994) collaborations. These alerts, and their further development by OGLE (Udalski 2003; Udalski et al. 2015b), became the basis for follow-up teams such as PLANET (Albrow et al. 1998), GMAN (Alcock et al. 1996), and MPS (Rhie et al. 1999), to conduct the first microlensing planet searches and so to find one of the first microlensing planets, OGLE-2005-BLG-390Lb (Beaulieu et al. 2006). Later, MOA began conducting a new survey and likewise almost immediately started to issue its own independent alerts (Bond et al. 2001). New followup groups formed, with μ FUN (Gould et al. 2010) in particular organizing itself around the new strategy proposed by Griest & Safizadeh (1998) of primarily monitoring high-magnification events because these had the highest sensitivity. This channel likewise led to one of the first microlensing planet discoveries, OGLE-2005-BLG-071 (Udalski et al. 2005). As we will discuss, this development was of particular note in the present context because events reaching high-magnification $A_{\max} \gg 1$ only remain near peak for $\sim 3t_E/A_{\max}$ during which time they should be monitored at very high cadence to fully exploit their high sensitivity to planets.

Beginning in 2014, a completely new application of microlensing alerts emerged: *Spitzer* microlensing (Gould et al. 2013, 2014, 2015a,b, 2016, 2017). By combining ground-based light curves with those obtained by *Spitzer* in solar orbit at ~ 1 AU, one can measure the so-called microlens parallax π_E ,

$$\pi_E \equiv \frac{\pi_{\text{rel}} \mu_{\text{rel}}}{\theta_E \mu_{\text{rel}}} \quad \theta_E^2 \equiv \kappa M \pi_{\text{rel}} \quad \kappa \equiv \frac{4G}{c^2 \text{AU}} \simeq 8.14 \frac{\text{mas}}{M_\odot}, \quad (1)$$

where $(\pi_{\text{rel}}, \mu_{\text{rel}})$ are the lens-source relative (parallax, proper motion), θ_E is the angular Einstein radius, and M is the lens mass (Refsdal 1966; Gould 1994b; Gould & Horne 2013). This measurement, by itself, provides a powerful constraint on the physical parameters M and π_{rel} (Han & Gould 1995), and, whenever θ_E is also measured, directly determines these quantities:

$$M = \frac{\theta_E}{\kappa \pi_E}; \quad \pi_{\text{rel}} = \theta_E \pi_E. \quad (2)$$

Because *Spitzer* is a narrow-angle instrument, it must be directed to point at *ongoing* microlensing events. This requires microlensing alerts. Moreover, in contrast to high-magnification microlensing alerts, which can be profitably exploited with even a few hours notice before the event peaks, *Spitzer* alerts require a long lead time simply because spacecraft commands are uploaded only once per week and must be delivered to *Spitzer* operations three days before upload. See Yee et al. (2015) and Figure 1 of Udalski et al. (2015a).

Because of this long lead time, the overwhelming majority ($> 90\%$) of *Spitzer* alerts have come from OGLE, whose excellent photometry and well-oiled alert machinery enable highly reliable microlensing alerts long before peak when the events are still usually very faint.

The Korea Microlensing Telescope Network (KMTNet, Kim et al. 2016) is presently the largest microlensing survey, but up until this point has not issued microlensing alerts. KMTNet consists of three identical 1.6m telescopes at CTIO (Chile, KMTC), SAAO (South Africa, KMTS) and SSO (Australia, KMTA), each equipped with a 4 deg^2 camera. This enables 24 hour coverage (weather permitting) of sky areas $\Omega = (12, 41, 85, 97)\text{ deg}^2$ at cadences $\Gamma \geq (4, 1, 0.4, 0.2)\text{ hr}^{-1}$, which are adequate to detect and characterize roughly (Earth, Neptune, Saturn, Jupiter) mass planets without followup observations. See Section 2 of Kim et al. (2018c) for more details on cadence as a function of area.

For this reason, microlensing alerts were initially a very low priority of KMTNet. Instead, after more basic tasks of commissioning the telescope and data pipelines were completed, the most urgent task was to develop a completed-event finder, which could identify microlensing events *after the season was completed* (Kim et al. 2018a,b,c). A microlensing event always leads to a temporary increase in brightness of the source. As such, it is characterized by at least three features: an increase in brightness relative to a baseline flux level, a peak, and a decrease in brightness relative toward the baseline. The event-finder algorithm is focused on detecting “completed events,” which have undergone all three of those phases.

For 2016 data, for example, these post-season events have yielded planets for three KMTNet-only events (Hwang et al. 2018; Ryu et al. 2018b; Zang et al. 2018), while also contributing critical data on planetary signals in events discovered by others (Mróz et al. 2017; Shvartzvald et al. 2017; Ryu et al. 2018a; Han et al. 2017a,b; Calchi Novati et al. 2018).

In contrast, an alert-finder algorithm would be required to detect events in progress without the benefit of all features. For example, a “rising event” is one that is before peak and for which the flux is simply increasing as a function of time. Thus, the algorithmic constraints are different than for the event-finder.

As discussed in some detail by Kim et al. (2018a), there are several reasons for KMTNet to develop an alert system. First, in contrast to its original design strategy of observing just 16 deg^2 at $\Gamma = 6\text{ hr}^{-1}$, which would have densely covered all caustic crossings whenever KMTNet was observing, the great majority of the area covered in the new strategy has cadences $\Gamma \leq 1\text{ hr}^{-1}$. This means that many caustic crossings, which typically last 1–2 hours, will be missed unless followup observations are organized for their predicted times.

Second, as mentioned above, the relatively rare high-magnification events can always benefit from higher cadence. This is particularly true for the new strategy because at $\Gamma \leq 1\text{ hr}^{-1}$, it is rather unlikely that planetary perturbations at high magnification can be properly characterized. However, even under the old KMTNet observing strategy, there was a substantial chance that high-magnification events would not be fully characterized,

both because $\Gamma = 6 \text{ hr}^{-1}$ is still relatively low for these events and because high-magnification events are more likely to be saturated ($I \lesssim 13$) or at least in the non-linear regime ($I \lesssim 13.5$) in KMTNet data.

Finally, KMTNet alerts could potentially contribute to finding *Spitzer* targets. This is particularly true in the northern Galactic bulge where extinction is generally higher and where OGLE generally observes at much lower cadences than KMTNet. Higher extinction means that at fixed optical brightness, the sources are brighter in *Spitzer*, making them more favorable targets. At least as judged by the “completed-event finder” results for the BLG14 field for the 2016 season¹, KMTNet finds many more events in the northern bulge compared to OGLE, which is not the case in the southern bulge.

2. Scientific Objectives and Practical Constraints

Ideally, one would like to announce microlensing alerts for all events that can be distinguished from “noise” (whether instrumental or astrophysical) based on a survey’s data, and to do so as soon as the data in which they are first distinguishable from noise are taken. This goal is in fact very nearly achieved by the MOA alert system: images are reduced on site within minutes after they are taken, and new sources are automatically identified and shown to team members. Then, after team review, which can be quite rapid in urgent cases, the events are publicly announced.

However, a variety of practical constraints prevent such an approach from being applied to KMTNet data, most of them related to the fact that the KMTNet system has roughly 12 times more pixels than MOA. Due to the sheer volume of data from KMTNet, the practical constraints due to finite resources must be taken into account in both the design and implementation of an alert-finder algorithm. Therefore, in devising an alert system, it is essential to begin by prioritizing scientific objectives and weighing these against practical constraints.

2.1. Scientific Objectives

The only science objective for the KMTNet alert system is to enable followup observations of ongoing microlensing events, either by *Spitzer* or from the ground. The OGLE and MOA alerts, by contrast, are also the principal means by which these groups publicly

¹<http://kmtnet.kasi.re.kr/ulens/event/2016/>

identify microlensing events. However, for KMTNet, this latter function is served by the event-finder, which finds events that are too faint to be detected by any reasonable alert algorithm.

Nevertheless, although the science objective appears unitary, it still must be further parsed in order to be properly weighed against practical constraints. As outlined in Section 1, follow-up observations can be triggered in pursuit of several different goals, with the main ones being

- 1) Monitoring by *Spitzer*
- 2) Monitoring high-magnification events
- 3) Monitoring identified planets
- 4) Monitoring predicted caustic crossings

The first two applications virtually require that the alert be issued before peak. In the case of high-magnification events, this is an absolute requirement. For *Spitzer* observations the requirement is “almost absolute” because the minimum 3-day delay between upload and first observation, combined with the fact most events peak earlier as seen from *Spitzer* than from Earth, together imply dramatically reduced probability of measuring the microlens parallax for events that are alerted after peak.

The last two applications require only that the alert be issued prior to the appearance (or, strictly speaking, the completion) of the anomaly *and* that this anomaly be recognizable in the publicly available light curves that can be accessed from the alert webpage. These applications clearly favor alerts before peak (as half of all anomalies occur before peak), but they do not absolutely require it.

2.2. Practical Constraints

The main practical constraints all basically derive from the volume of data combined with the limited computational and human resources to deal with these data. KMTNet makes approximately 10^{12} photometric measurements per season, distributed over 5×10^8 catalog stars within a total of 27 fields of 4 deg^2 . Each of its three cameras has 3.4×10^8 pixels distributed over four chips. Note that slightly less than 10% of all KMTNet observations are in *V* band. These are not used for alerts (nor for post-season event-finding) and so are not reduced in real time.

The first constraint is that the photometric pipeline must be able to “keep up” with the data flow. That is, the data should be processed at a rate that is equal to or faster than the mean rate at which they are acquired. We have placed “keep up” in quotation marks because there will inevitably be some delay between the time that the data are taken and the time that they are reduced and archived, which we discuss in some detail further below. However, what is important in the present context is that this delay be small compared to the duration of a typical microlensing event. That is, the reductions must be basically concurrent with the observations and, in particular, at the height of the microlensing season this requirement would be that the delay cannot increase due to increasing backlog of unprocessed observations. While this constraint may perhaps seem too obvious to even mention, in fact, the KMTNet pipeline only began catching up with the observations in mid-May 2018. For example, the reductions of 2017 KMTNet data did not begin until December 2017 and were not completed until three months later. See the discussions in Kim et al. (2018a,b). Moreover, the onset of reductions of 2018 data were delayed by 2 months due to a massive upgrade of the star catalog (Kim et al. 2018c), and by the evaluation of the statistical characteristics of these catalog stars, which is required for efficient real-time selection of microlensing events (Section 3.2). Hence, prior to 2018, an alert system would not have been possible. Moreover, as we will describe in Section 5, the problems engendered by this “catching up” will both impact the inaugural phase of KMTNet alerts and are likely to impact the continued functioning of this system.

The second constraint is a problem of data input/output (I/O) rates and storage. In order to reliably detect microlensing events, all 10^{12} measurements (or whatever fraction have been acquired by a particular date) must be readily available on storage disks local to the computers applying the algorithm. This requires large hard disks. In principle, the required storage could be reduced using a tiered system, in which a subset (say the previous month) of the data has immediate local availability and the rest can be acquired from more distant storage at a more leisurely pace for the handful of events that are identified from the recent-month of data as “interesting”. In practice, such a tiered system would be unwieldy and prone to failures. As we will show below, 8 bytes are required to store one measurement. Hence, simply to access the data requires 8 Terabyte of rapid-access memory. In fact, KMTNet possesses eight 2-Terabyte solid state disks (SSD), two attached to each server that is responsible for processing one of the four chips on the camera. Hence, this requirement is satisfied by the KMTNet system. In particular, no tiered system is required.

The third constraint is that at some point, a human must review all candidate alerts to assess the probability that they are real microlensing events. This affects both the relevant timescales (below) and the efficiency and reliability requirements of the algorithm.

The remaining constraints all relate to the timescale for the complete alert-finder process to run from start to finish, i.e., the turnaround time from the acquisition of photometric measurements to the human review of updated light curves that determines which light-curve variations should be announced as “clear” or “probable” microlensing. Whichever step takes the longest will determine this turnaround time, which in turn will enable and/or limit the scientific applications.

For KMTC and KMTA, images are transferred from the camera to Korea within a few minutes of the time they are taken. Due to lower band width from South Africa, the arrival of the final KMTS image for a given night can be delayed by up to 6 hours after it is taken, depending on a variety of factors but mainly the season. In particular, ~ 6 hour delays are typical for the entire peak season from May through August.

Once they arrive, images are pre-processed (cross-talk correction, de-biasing, flat-fielding, bad-pixel masking, and writing to disk) in about two minutes on average, using eight processors that are reserved for this purpose. Aligning and subtracting images requires 4 minutes, and DIA photometry requires 5 minutes. Another 1 minute is required to append these photometric measurements to the individual light-curve files. Therefore, for KMTC and KMTA, the total time from image acquisition to photometry is well under one hour, but for KMTS these processes often require up to seven hours due to the delay in transferring the data.

These constraints imply that there are three potential timescales that are relevant for the machine review (i.e., machine-based vetting prior to human review) of light curves: one hour, 12 hours, and 24 hours. That is, machine reviews taking substantially less than one hour are not useful because the basic reductions already take a significant fraction of an hour. Machine reviews taking 12 hours would enable two human reviews per day, one at about UT 21:00, i.e., roughly 12 hours after the arrival of KMTS and KMTC data, and one at UT 07:00, i.e., roughly 12 hours after the arrival of KMTA data. Conveniently, these would be at the beginning and end of the Korean work day. Finally, an alert-finder algorithm taking less than 24 hours would permit daily human reviews, which would be well matched to the human diurnal cycle.

3. Alert Algorithm

From a conceptual standpoint, the alert-finder algorithm works as follows:

Every light curve is examined by machine to determine whether it is consistent with a rising microlensing event. It is checked to see if there is an increase in brightness over the baseline level, i.e., by evaluating whether there have been at least N_{high} recent consecutive

points that were more than 3-sigma above the median. Then, those light curves with such a sustained increase in brightness are fitted with a “rising microlensing light-curve model” and compared to a flat line, i.e., by evaluating $\Delta\chi^2$ relative to a $\Delta\chi^2_{\text{thresh}}$ threshold. Events passing those metrics are vetted for duplicates and variables. Finally, they are reviewed by a human operator to determine which events are real microlensing events. The entire process prior to review by a human operator constitutes a “machine review.”

However, as discussed in Section 2.2, there are a number of practical considerations that affect the implementation of this concept. The biggest one is the enormous data volume compared to limited computational and human resources. There are also complexities introduced by the fact that the data come from three distinct sites, each of which have different observing properties and different rates of data transfer. We discuss the practical implementation of the algorithm and its implications below.

3.1. Qualitative Characteristics

The considerations described in Sections 2.1 and 2.2 imply that the machine review should focus on and robustly identify rising (i.e., pre-peak) events, should operate as rapidly as possible, and should minimize the number of false positives in order to permit rapid human review. Each of these “positive” goals implies some “negative” cost.

“Focusing on rising events” implies possibly foregoing the detection of events that have already peaked. Because all events must rise before they peak, it may appear that this is no cost at all². However, low-amplitude events may not contain enough information for reliable detection before peak and yet may acquire such information after peak. The choice being made is to forgo these events as alerts. First, these events will be found at the end of the season by the event-finder. Second, as discussed in Section 2.1, most of the scientific driver for alerts comes from pre-peak alerts. Third, events that are so noisy that they cannot be reliably identified before peak are unlikely to give rise to recognizable anomalies that lead to followup observations after peak.

“Operating as rapidly as possible” means minimizing the number of data points examined for each light curve and then, on this basis, selecting only a small fraction of all light curves for more intensive analysis. This implies, in particular, that noisy light curves whose microlensing signature is only recognizable by averaging over a very large number of points will be missed. Again, the rationale for this choice is that such events will be found by the

²Here, we are ignoring events that peak between seasons. We address these in Section 5.

event-finder at the end of the season and that such events are much less likely to give rise to identifiable anomalies that would trigger followup observations.

“Minimizing the number of false positives” implies setting the machine threshold high enough that some real events will be missed and hence will not be shown to the operator. By contrast, the event-finder has a relatively low machine (event-detection) threshold. However, in that case, human review is required only once per year, not once or several times per day.

3.2. Two Machine-Review Requirements to Trigger Human Review

Based on the qualitative characteristics described in Section 3.1, we demand that a light curve satisfy the following two quantitative requirements to pass on the stage of human review:

- A1) At least N_{high} “consecutive” flux measurements that are $\geq 3\sigma$ above the median
- A2) $\Delta\chi^2 > \Delta\chi^2_{\text{thresh}}$ improvement for a “rising microlensing light-curve model”

Note that requirement (A1) preferentially suppresses (though it does not eliminate) variable stars because their “scatter” is typically dominated by astrophysical (rather than Poisson or instrumental) variations. The practical implementation of these two conditions will be described in Section 3.3, but first, several terms within these conditions require further explanation.

The term “consecutive” is placed in quotation marks because its definition is fairly complex. First, we mask any point that fails to meet any one of the following three conditions

- B1) Background light below the 92nd percentile
- B2) Seeing below the 84th percentile
- B3) $\chi^2(\text{DIA-PSF fit})$ below 100

These three statistical quantities, as well as the median and σ of the flux from (A1), are all derived from previous seasons (currently the 2016 season is the reference) and are observatory-specific and specific to this particular star. Note also that the “ σ ” in (A1) is actually one-half of the difference between the 84th percentile and the 16th percentile of the previous seasons’ flux (i.e., it is not the photometric uncertainty). These statistics are cataloged and are not recomputed for each application of the algorithm.

Second, the N_{high} points can be “consecutive” within any combination of the $3N_{\text{fields}}$ light-curve files. That is, the event may be observed in several (“ N_{fields} ”) overlapping fields, and for each of these it is observed from three observatories. There are $i = 1, \dots, (2^{3N_{\text{fields}}} - 1)$ combinations of light-curve files (so $N_{\text{fields}} = 1$ has 7 combinations including, for example, KMTC alone or in combination with KMTS and/or KMTA.). For each of these, we write i as a binary number with $3N_{\text{fields}}$ digits (i.e., each digit represents a light curve, which is either under consideration or not). Then, in asking whether there are N_{high} consecutive points, we consider only the light-curve files for which the entry in this binary representation is “1”, and ignore files for which the entry is “0”. For example, this number is “101” for $i = 5$ and $N_{\text{fields}} = 1$, and only two out of three light-curve files are considered.

The “rising microlensing light-curve models” for the flux F are defined as

$$F(t) = a_0 + a_1(t - t_{\text{rise}})\Theta(t - t_{\text{rise}}), \quad (3)$$

where Θ is a Heaviside step function and a_1 is constrained to be positive. Note that Equation (3) has only one non-linear parameter (t_{rise}). Hence, a good estimate of the best fit can be obtained by carrying out a two-parameter (a_0, a_1) linear fit on a one-dimensional discrete set of models characterized by different t_{rise} . The $\Delta\chi^2$ improvement is then measured relative to a flat model, i.e., $F(t) = a_0$.

3.3. Practical Implementation

Before assessing how well these two machine-review requirements (A1) and (A2) satisfy the scientific objectives and practical constraints, it is first necessary to describe their practical implementation.

Because of the data volume, the system for storing light-curve data substantially affects the speed of the alert-finder algorithm. For example, it is significantly faster to access information stored in binary rather than in ASCII format. Thus, in discussing practical implementation, we must begin by describing how light-curve data is stored.

Light curves are organized by “patches”. There are 64 slightly overlapping patches per chip, each of which is 1 deg^2 . Within each patch, all the light curves have exactly the same length and exactly the same epochs. If a particular photometric measurement fails for any reason, it is flagged but left in the file. Therefore, there is only one date file (and also only one background-light file) for each patch, which are read into memory at the start of processing the patch. The remaining variables describing each photometric measurement are the difference flux, the flux error, the χ^2 of the DIA fit, and the seeing. These require a total of $4 \times 2 = 8$ bytes in the direct-access binary-format files. The flux F is stored as

the nearest (2-byte) integer of a modified “Lupton magnitude”, $K_F = 3000 \sinh^{-1}(F/3000)$, the flux error is stored as the nearest (2-byte) integer, and the remaining two parameters are multiplied by 100 and then stored as 2-byte integers. The flux units are in ADU, with 1 ADU corresponding to $I \simeq 28$. Therefore, storing the modified Lupton magnitude and the flux error to the nearest integer does not induce any significant loss of precision.

The vetting program has three input parameters, the χ^2 threshold $\Delta\chi^2_{\text{thresh}}$, the number of consecutive “high” points (N_{high}) required to trigger a deeper investigation, and the last date of data reviewed in the previous search (which, to first approximation, is set as the earliest of the previous upload dates from the three observatories, but see below). We adopt $\Delta\chi^2_{\text{thresh}} = 400$ for fields with $\Gamma \geq 1 \text{ hr}^{-1}$ cadence and $\Delta\chi^2_{\text{thresh}} = 250$ for fields with $\Gamma \leq 0.4 \text{ hr}^{-1}$ cadence. For the first, we find from practical tests that very few candidates can be reliably identified as even “probable microlensing” (i.e., the minimum requirement for them to be publicly announced) at $\Delta\chi^2 < 400$, and of those that can be, almost none are identifiable at $\Delta\chi^2 < 350$. Moreover, extremely few of those that could be identified at $\Delta\chi^2 < 400$ and do not reach $\Delta\chi^2 > 400$ within a day or so, prove to be worthy of followup observations. However, for the lower-cadence fields, we find that reliable alerts (i.e., “probable” or “clear” microlensing) are often possible at or just above $\Delta\chi^2 = 250$.

We choose $N_{\text{high}} = 10$ for fields with $\Gamma \geq 1 \text{ hr}^{-1}$ cadence and $N_{\text{high}} = 5$ for fields with $\Gamma \leq 0.4 \text{ hr}^{-1}$ cadence. Below these thresholds, we find that the number of spurious candidates rises dramatically. See Figure 12 of Kim et al. (2018a) for the cadences of each field.

The last parameter (last date of review) is, of course, updated for each operation of the program. In fact, the “last date of review” is a rather complex quantity, in part because it is actually the date of the last observation available at the time of the review. Thus, the three different observatories necessarily have different “last dates”. Nor is it a viable solution to simply keep track of these three dates separately. In order to consider strings of consecutive points from multiple observatories, one must have a common “last date”. We note that there is no fundamental harm in setting this date arbitrarily far back in the past: this only increases operation time. Therefore we set this date conservatively to make sure that no instances of N_{high} consecutive points are missed. We first evaluate the last date for each observatory, $t_{j,\text{last}}, j = 1, 2, 3$. We then set

$$t_{\text{last}} = \max[(t_{\text{now}} - 4 \text{ days}), \min(t_{j,\text{last}})] \quad (4)$$

where t_{now} is the most recent observation from any observatory. The first condition ($t_{\text{last}} \geq (t_{\text{now}} - 4 \text{ days})$) guards against duplicating the same searches every day for cases of long spans of bad weather at one observatory. Finally, we set $t_{\text{last}} = (t_{\text{now}} - 4 \text{ days})$ for t_{now} within one day of the full moon in order to guard against gaps in usable data due to many consecutive data points that violate condition (B1).

At the present time, we analyze the three sites together but each field separately, i.e., $N_{\text{fields}} = 1$, for reasons that we discuss in Section 5.

The two requirements (A1) and (A2) are implemented through three steps, with the first two steps corresponding to the first requirement and the last step corresponding to the second.

3.3.1. Step 1: Vetting for N_{high} points

The program begins by stepping through each data file, starting at the “bottom” (last data entry) and including $N_{\text{high}} + 10$ points before t_{last} . It counts the number of points from all data files combined that satisfy the three conditions B1–B3, and for which the flux is at least 3σ above the median. If this number is at least N_{high} then it moves on to the second step.

The great majority of light curves fail this test. Because the test is simple and typically requires reading only a few dozen points, it is very fast.

3.3.2. Step 2: Vetting for N_{high} consecutive points

A light curve that passes Step 1, is then fully tested for requirement (A1). First, an internal list is created that consists only of the points identified in Section 3.3.1 that satisfy conditions B1–B3. The list combines data from all three files and is ordered by date, and with the data file from which the data point was drawn marked. Data points that are at least 3σ above the median are flagged as “high”, while the others are “not high”. The program then goes through this list $i = 1, \dots, 2^{N_{\text{files}}} - 1$ times as described in Section 3.2 to check if any combination of files has N_{high} consecutive “high” points.

A substantial majority of stars that pass Step 1, fail Step 2.

3.3.3. Step 3: Vetting for rising microlensing light curve

Stars that pass Step 2 are checked to see if they have “rising microlensing light curves” as characterized by Equation (3). For this purpose, the *entire* light curve for the season is read into memory, i.e., typically of order 100 times more data than in Steps 1 and 2. Again, data points failing to satisfy conditions B1–B3 are flagged and ignored. Then a series of

$k = 1, \dots, N_{\text{fit}} = 16$ fits are carried out, which are defined by

$$t_{\text{rise}} = t_{\text{now}} - 2^{(k-3)/2} \text{ day}, \quad (5)$$

where t_{now} is the most recent observation. Hence, $(t_{\text{now}} - t_{\text{rise}})$ spans a range from 0.5 to 90.5 days. The fitting procedure is similar to the one described by Kim et al. (2018a) for their much more extensive set of models (~ 5000 versus 16). Each fit is carried out four times. First, all the data (from all $N_{\text{files}} = 3N_{\text{fields}}$ files) are fitted to derive the $a_{m,j}$ ($m = 0, 1$, $j = 1, \dots, N_{\text{files}}$), i.e., $2N_{\text{files}}$ parameters. Second, the χ^2 contribution of each data point is evaluated. The 5% worst data points from each file are eliminated. Third, all data files are refitted with these points removed in order to redetermine the $a_{0,j}$ and $a_{1,j}$. Fourth, the $\chi_{j,2\text{-parm}}^2$ of each data file is evaluated.

The same surviving data points (from the second fit) are then fitted to a flat line, $F_j(t) = a_{0,j}$, $\chi_{j,1\text{-parm}}^2$ is evaluated for each data file, and hence $\Delta\chi_j^2 = \chi_{j,1\text{-parm}}^2 - \chi_{j,2\text{-parm}}^2$. Finally, we evaluate $\Delta\chi^2 \equiv \sum_j \Delta\chi_j^2 \Theta(\Delta\chi_j^2)$ and accept the light curve for human review provided that $\Delta\chi^2 > \Delta\chi_{\text{thresh}}^2$.

Note that whereas Kim et al. (2018a) removed the 10% worst points, we are only removing the 5% worst. This is because we are already removing bad-seeing and high-background points as part of our general procedures.

As for the event finder (Kim et al. 2018a), we subtract the contributions to $\Delta\chi^2$ of the two points from each data file that contribute the most to $\Delta\chi^2$ before comparing the result to $\Delta\chi_{\text{thresh}}^2$. This guards against short-term artifacts.

3.4. Group Finding

After all candidates have been selected from a patch, a “friends-of-friends” algorithm is applied to group together neighboring light curves that are morphologically similar. This algorithm is very similar to the one used for the event-finder (Kim et al. 2018a) except that the “friend” condition is necessarily different because the ensemble of models is different. In this case, (in addition to demanding that the star positions be within $4''$) we require that $|\log[(t_{\text{now}} - t_{1,\text{rise}})/(t_{\text{now}} - t_{2,\text{rise}})]| < 0.2$, where $t_{1,\text{rise}}$ and $t_{2,\text{rise}}$ are the rise times of the models for the two candidates. That is, $|k_1 - k_2| \leq 1$. The group member with the highest $\Delta\chi^2$ is the designated as the “group leader”. Only the group leader is further considered.

3.5. Automated Post-Machine-Selection Vetting

The status of many (generally, a substantial majority) of “group leaders” identified by the grouping algorithm are already known, and hence it is not necessary to show them to the operator. That is, they are already-known microlensing events (which do not require “rediscovery”) or they are already-known variables or artifacts.

Candidates that are registered as “clear microlensing” (see Section 3.6) during a given year are automatically suppressed prior to visual review for the rest of the year. Similarly, candidates that are registered as “not microlensing” are also suppressed, in this case for all future years as well.

In addition, all stars that were found to be “variables” or “artifacts” in any application of the event-finder (Kim et al. 2018a,c) from previous years, or to be a member of a “group” whose “group leader” was so designated, are likewise removed from the visual review.

3.6. Visual Review

The visual review of events is broadly similar to that of the event-finder (Kim et al. 2018a), but with a number of particular features that are specific to real-time microlensing alerts.

As with the event finder, the operator is shown a four-panel display in which the separate light-curve files are aligned via the model parameters, with the model (a broken line) also shown. The upper-left panel shows the most recent data, going back twice as far in time as t_{rise} (but as least 5 days before t_{rise}) and with a range of fluxes that goes $\pm 3\sigma$ beyond the range of the model. This provides the main information on whether the data appear consistent with a rising microlensing event. The upper-right panel shows the same time range but the vertical axis encompasses the full range of fluxes observed during this interval. This is similar to the event-finder display and allows one to check for anomalies, which would be an important signature of microlensing in cases for which the light curve in the upper-left panel appears irregular. The lower-right panel contains the full year of data taken so far with the same flux range as the upper-left panel.

The biggest difference in this alert display relative to the event-finder display is the lower-left panel. This shows the earlier-year (currently 2016) data aligned according to the current-year model. For real microlensing events, this will usually be flat, and the model-induced alignment will produce roughly coincident (and flat) light curves for the earlier year. However, for artifacts (due for example to bleeds from saturated stars), the alignment can

be a strong function of the different conditions at different observatories and so can easily yield misaligned 2016 light curves. This is an important signature of artifacts.

Figure 1 shows the four-panel display for a candidate that was judged to be an artifact.

All visually-reviewed light curves are given one of the following four classifications:

- C1) Clear microlensing
- C2) Probable microlensing
- C3) Possible microlensing
- C4) Not microlensing

Events classified as C1 and C2 are added to the web page of “public alerts”, with a flag indicating whether they are “clear” or “probable”. As discussed in Section 3.5, events classified as C1 and C4, are suppressed for future applications of the program because the status of these events is considered already known. On the other hand, future re-appearances of candidates marked C2 or C3 are labeled as such in the display, as a reminder in preparation for their possible reclassification based on new information. In particular, if a C2 candidate is upgraded to C1 or downgraded to C3 or C4, then this is marked on the webpage.

3.7. Evaluation of Algorithm in Light of Objectives

In Section 3.1, we outlined three qualitative goals for the alert system that were derived based on the scientific objectives and practical constraints discussed in Section 2. These were (in permuted order) “operate as rapidly as possible”, “focus on and robustly identify rising events”, and “minimize the number of false positives” presented to the operator.

Here, we evaluate the practical implementation described above in light of these goals.

The most crucial goal is the first: “operate as rapidly as possible”. Each of up to 5×10^8 light curves must be reviewed, and these receive typically 1–100 additional data points per day, with a median of ~ 8 . The time-limiting step is the initial review of these 5×10^8 light curves, which the algorithm carries out by checking for at least N_{high} points since the previous review (plus $N_{\text{high}} + 10$ additional points). That is, for daily reviews, the processing time is dominated by reading in 15–100 records, with a median of ~ 25 .

This seems modest but it should be compared against another scheme that is in fact roughly 2–3 times as fast for the case of only one date file ($N_{\text{files}} = 1$). In this alternate

scheme, each star is assigned a counter K_{high} , which is the number of consecutive high points ending on the most recent observation. Then, when a new (for example, 24-hr) set of data are acquired, each successive data point is examined. If the data point is high, then $K_{\text{high}} \rightarrow K_{\text{high}} + 1$, and if not, then $K_{\text{high}} \rightarrow 0$. Additional investigation is then triggered if $K_{\text{high}} \geq N_{\text{high}}$. The main time saving comes from not reading any additional past records.

However, this approach is not easily generalized to the case of multiple files, in particular coming from multiple observatories. Ultimately (Section 3.3.2), we trigger on N_{high} points in any one of $N_{\text{comb}} = (2^{N_{\text{files}}} - 1)$ combinations of files, i.e., a minimum of seven combinations for $N_{\text{files}} = 3$. The reasons for this will be discussed below, but here we focus on the implications for speed in the alternate scheme that we are currently discussing. First, it means that one would require N_{comb} counting parameters $K_{l,\text{good}}, l = 1, \dots, N_{\text{comb}}$. Second, it would require time-sorting the data from all files in order to update these N_{comb} counting parameters. Even at the minimum of $N_{\text{comb}} = 7$, this would be cumbersome. Moreover, it would become completely unmanageable when the process is upgraded to combine overlapping fields, which reaches up to $N_{\text{fields}} = 4$ ($N_{\text{comb}} = 4095$) for a considerable number of stars (Kim et al. 2018a). Therefore, such a system would be at most marginally faster under our initial implementation and would not be upgradable.

The total time for Steps 2 and 3 of the alert-finder algorithm is small compared to Step 1 primarily because the fraction of stars that pass Step 1 is small. In principle, the modeling (Step 3) could take a substantial amount of time if many models were considered because (in contrast to the much more numerous event-finder models of Kim et al. 2018a) the entire light curve is modeled. However, because we consider only 16 models, most of the time spent on this step is just reading in the full light curve files. This requires, on average, about 30 times more reads than Step 1. However, because $< 1\%$ of all light curves reach Step 3, the total time spent on this step is still substantially smaller than on Step 1.

The next qualitative goal is to “focus on and robustly identify rising events”. Because the Einstein (1936) magnification $A(u) = [1 - (u^2/2 + 1)^2]^{-1/2}$ rises rapidly inside the Einstein radius ($u < 1$) and quickly goes to $A \rightarrow 1$ outside ($u > 1$), Equation (3) is essentially always a reasonable model for rising single-lens microlensing events. Note that it is not necessary for the model to be a “good fit” by some particular standard. All that is necessary is that it be substantially better than a flat line. However, this model is also quite reasonable for the beginning rise of almost all binary lenses. Most of these look qualitatively like single-lens events. However, even those that become visible by an abrupt jump into a caustic trough are still much better represented by Equation (3) than by a flat line. Moreover, in this modeling, the whole light curve is fitted (with outlier rejection), so that points that grossly deviate from the pattern (whether due to noise, systematics, or binary-lens signatures) cannot by

themselves cause automated rejection of the candidate. Figure 2 shows the four-panel display corresponding to the initial selection of binary lens KMT-2018-BLG-0061, while Figure 3 shows the full re-reduced pySIS light-curve for this event as it subsequently developed. Hence, Step 3, in itself, is quite robust at retrieving real microlensing events for visual review.

The key question is then whether real microlensing events will be rejected at Step 2 (N_{high} consecutive high points). For events that rise very quickly, so that suddenly the light curve is much more than three “typical sigma” above the median, essentially all data points will be “high” and it is important to combine all data files in order to register this as rapidly as possible. This is particularly true for short events. On the other hand, for slowly-rising light curves, data problems at one or more observatories can easily break consecutive streaks of high points. Therefore, the most robust way to deal with all contingencies is to search for N_{high} consecutive high points in *any* combination of data files. By practical experimentation, we found $N_{\text{high}} = 5$ provides adequate guard against spurious high points triggering false candidates for $\Gamma \leq 0.4 \text{ hr}^{-1}$, but this limit is not adequate for higher-cadence fields. These require $N_{\text{high}} = 10$. These restrictions imply that roughly one day of data that is “significantly more than 3σ high” is usually required to trigger Step 3. And this in turn implies diminishing returns for running the alert system more than once per day.

4. KMTNet Alert Webpage

As soon as the visual review of alert candidates is completed on a given day, the full list of candidate classification is sent to a script that controls two processes: webpage update and initiating pySIS photometry (Albrow et al. 2009). First, all previously identified candidates are checked for possible updates in their classification. Second, new pages are created for each of the events that are newly classified as “clear” or “probable” microlensing, and a link to that page is created on the cover page, which contains a list of the event names, coordinates, classifications, estimated I -band extinction, and an estimate of the event parameters. The page initially contains the 4-panel DIA-based display that led to selection, links to the underlying DIA data, a finding chart, the event parameters and coordinates, and cross-identifications with known OGLE and/or MOA events.

Simultaneously, the script places the event on the queue of targets to obtain pySIS photometry from an automated pipeline. In contrast to the DIA photometry, which currently is drawn from a single field, the pySIS photometry includes data from all overlapping KMTNet fields that contain the event. As soon as this photometry is complete, the page is updated to include a figure showing the pySIS light curve together with a microlensing model, as well as links to the pySIS data. As additional data are taken, the pySIS figure and data files are

updated as soon as they are reduced by the same automated pipeline.

5. Ramp-Up of KMTNet Alerts

KMTNet alerts will be introduced gradually in 2018 according to a scheme that is fundamentally governed by the availability of reduced real-time data. There are three reasons for adopting this ramp-up approach, rather than waiting for the system to be “fully functioning”. First, alerts for *Spitzer* are needed immediately. Second, we hope to improve the system by getting feedback before it is fully functional. Third, as we discuss below, it is quite possible that the system will still be only “mostly functional” in 2019. Hence, waiting for “full function” could be counterproductive.

As discussed in Section 2.2, 2018 data reduction did not begin until about 1 May 2018. Prior to this time, the alert software was tested on blinded data from 2016 and 2017. After 1 May, all reduction efforts were concentrated on five northern bulge fields, BLG14, BLG15, BLG18, BLG19, and BLG16. The first four of these are the most likely to be productive for *Spitzer* alerts due to high event rate, high extinction, and relatively low cadence of OGLE observations. Those four all have cadence $\Gamma = 1 \text{ hr}^{-1}$, so BLG16 was added to gain experience with a $\Gamma = 0.4 \text{ hr}^{-1}$ field. As these reductions proceeded, more realistic testing and trial runs were done on the 2018 BLG14 data, gradually expanding to a few other fields. We populated the webpage with all of these “alerts”, although no one outside of KMTNet was “alerted” at this time. Following a two weeks of this realistic testing, we made the page public at <http://kmtnet.kasi.re.kr/ulens/event/2018/>, which includes the above “alerts” from the test phase, as well as all subsequent real alerts.

5.1. Limitations Due to Data Processing Rate

For 2018, we will continue to update photometry on all fields that have previously been “caught up”, and we will use the computer time that remains to “catch up” on additional fields, one at a time. After each such field is caught up, we will begin real time alerts on that field. As we discuss below, however, we think that it is likely that alert coverage in 2018 will be mostly restricted to the Northern bulge.

At present the image analysis proceeds at about 57% of the peak (i.e., June/July) time-averaged *I*-band data-acquisition rate. This (together with the fact that 2018 DIA reductions only began in May) is the fundamental reason that alerts will be restricted to a modest fraction of the total KMTNet area in 2018.

As mentioned in Section 2.2, it takes 5 minutes to do photometry on one image. Ninety-six processors are assigned to this process (actually, 24 processors per server for each of four servers), while 64 other processors are simultaneously working on the previous step (alignment and subtraction) for the next set of images. However, I/O and computational constraints prevent any wider distribution of the processing. This means that the average rate of image processing is one per five minutes, or 288 per day. During June and July, we take about 24 *I*-band images per hour for about 9.4 hours per night at each of the three observatories. This is about 675 images per day provided that there is good weather at all sites, or about 500 images per day allowing for weather and equipment problems.

Moreover, in the absence of additional computers or greater algorithmic efficiency, we will not be able to keep up with the full data flow at peak season in future years. This problem can be significantly ameliorated, though not completely solved, at relatively low-cost by gradually curtailing reductions of the three overlap fields BLG41, BLG42, and BLG43 beginning about 1 April until these reductions are completely halted about 1 May. These three fields consume about 27% of observation time, but they only cover about 1 deg^2 that is not covered by other fields (primarily BLG01, BLG02, and BLG03). For the remaining 11 deg^2 covered by these fields, the data are very important for finding and characterizing planets, but are not crucial for issuing alerts.

This still leaves 3.5 months (1 May to 15 August) when real-time data reduction cannot keep pace with data acquisition. In the absence of other solutions, the approach would be to leave KMTA data partially (beginning 1 May) or totally (beginning 1 June) unreduced for this period and to search for alerts based only on KMTC and KMTS data.

Based on these qualitative considerations, we adopt the following algorithmic approach to deciding the next image to process from a possibly accumulating backlog:

D1) Observatory order: KMTC, KMTS, KMTA

D2) Field Order: BLG(14,18,15,19,11,38,16,20,12,02,03,01,04,17,22,35,31,37,21,32,33,34,13,36)

D3) Earliest epoch that is not yet processed

D4) If no unprocessed images from fields BLG01–38, then

D4.1) Observatory order: KMTC, KMTS, KMTA

D4.2) Field Order: BLG(42,43,41)

D4.3) Earliest epoch that is not yet processed

The field order shown in (D2) prioritizes Northern Bulge fields, which will continue to be important for *Spitzer* alerts in 2019. The order could be changed to meet future changes in priorities.

This algorithm (D1 – D4) automatically implements the qualitative features described above. The key question is how it functions in practice, in particular during the roughly six weeks when each observatory can observe about 9.4 hours per night.

The first point is that whenever KMTC is observing (which is a substantial majority of the time), there will be continuous new data in all fields, which will enable the selection of new alerts. That is, because of condition (D1), KMTC data will always be reduced within a few hours of the time they are taken. Second, if KMTC and KMTS experience intermittent bad weather, then both observatories will remain approximately caught up. Then, if KMTC weather turns bad but KMTS continues to observe, the most recent KMTS images will be processed within seven hours after they are taken.

The first major “problem” with this algorithm occurs if KMTC and KMTS have extended simultaneous good weather. For example, after one week of joint good weather, KMTS would be four days behind in its processing. However, due to condition (D2), this backlog would not be uniform over all fields. Rather, fields BLG14, BIG18, BLG15, BLG19, BLG11, BLG38, BLG16, and BLG20 would be completely caught up, while the remaining fields would be a week behind. Hence, new alerts could be immediately identified from these fields, but not the others. Then, as bad weather continued at KMTC, the remaining KMTS fields would successively catch up in the order specified by (D2). In the extreme case of all bad weather at KMTC and all good weather at KMTS, it would take about nine days for KMTS to fully catch up. However, in more typical scenarios, this catch up would be much faster. For example, with two days of good weather at KMTS followed by two days of bad weather, KMTS would be completely caught up. Thus, for the great majority of the time that either KMTC or KMTS is operating, there can be near real-time alerts over all, or essentially all fields.

The real difficulty comes when both KMTC and KMTS have simultaneous bad weather. Let us consider that this occurs four weeks into the six-week period of 9.4-hour observability. Then all KMTA fields will be at least four weeks behind (and the lower priority fields more than this). This dual hiatus would immediately trigger reductions of KMTA BLG14, which will require about a half day to catch up. Hence, alerts can begin on this field with a half-day delay. For BLG18, the delay will be one day. Hence, there would be a gradual return of alerts beginning with the highest priority fields.

Thus, at the present time, this algorithm appears to be the best way to cope with

overtaxed computing resources at the peak of the season.

5.2. Potential Upgrades

Finally, we remark on two possible upgrades that are lower priority.

First, we note that two-thirds of the missing $\sim 1 \text{ deg}^2$ from fields BLG41, BLG42, and BLG43 mentioned above could be recovered by reducing the southern-most patches $[(1, i), i = 1 \dots 8]$ of the two northern chips (K and M) of fields BLG41, BLG42, and BLG43. These patches constitute just 1/16 of these fields and so require only about 2% of the total computing time. However, it is not clear at the present time whether the modest additional science output warrants the added complexity of reducing partial chips.

Second, as we mentioned in Section 3.1, by focusing on rising events, we are ignoring not only events that have already peaked during the year (and so will already have been alerted provided that they have significant signal) but also events that peaked between seasons and so may have strong “purely falling” signals. These could, in principle, be recovered by making one or two runs of a slightly modified version of the same program early in the season. There would be four modifications, all small. First, one would replace Equation (3) by

$$F(t) = a_0 + a_1(t - t_{\text{flat}})\Theta(-(t - t_{\text{flat}})). \quad (6)$$

Second, one would accept only fits with $a_1 < 0$. Third, one would test a grid of models in which $(t_{\text{flat}} - t_{\text{now}})$ was both positive and negative. Fourth, one would set the “previous date” to the beginning of the season. It would be quite cumbersome to include such fits during the 2018 ramp up, but it might be feasible near the beginning of 2019.

6. Disclaimer

As discussed in Section 2.1, the only scientific objective of the KMTNet public alerts is to encourage and enable followup observations that lead to better characterization of microlensing events discovered by KMTNet, including parallax measurements, discovery of new planets, and improved characterization of planets and binaries that are already recognizable.

We welcome cooperation with others who obtain such followup data, as well as with other surveys that obtain data on the same events. However, the KMTNet data that are displayed and linked on these pages are completely proprietary and cannot be published or reproduced in talks, conference proceedings, etc, without the express permission of KMTNet. As discussed by Kim et al. (2018a,b,c), all KMTNet light curves will eventually be made

public in a series of annual data releases. Our goal is that these releases should be made within well under a year of the end of each season. However, until the date of release, as specified in the data-release papers, these data remain completely proprietary.

Work by AG was supported by AST-1516842 from the US NSF. IGS and AG were supported by JPL grant 1500811. Work by C. Han was supported by the grant (2017R1A4A1015178) of National Research Foundation of Korea. This research has made use of the KMTNet system operated by the Korea Astronomy and Space Science Institute (KASI) and the data were obtained at three host sites of CTIO in Chile, SAAO in South Africa, and SSO in Australia.

REFERENCES

- Alard, C. & Lupton, R.H., 1998, *ApJ*, 503, 325
- Albrow, M. Beaulieu, J.-P., Birch, P., et al. 1998, *ApJ*, 509, 687
- Albrow, M. D., Horne, K., Bramich, D. M., et al. 2009, *MNRAS*, 397, 2099
- Alcock, C., Allsman, R., Axelrod, T., et al. 1994, *IAUC* 6068
- Alcock, C., Allsman, R., Alves, D., et al. 1996, *ApJ*, 463, 67
- Beaulieu, J.-P. Bennett, D.P., Fouqué, P. et al. 2006, *Nature*, 439, 437
- Bond, I.A., Abe, F., Dodd, J.R., et al. 2001, *MNRAS*, 327, 868
- Calchi Novati, S., Suzuki, D., Udalski, A., et al. 2018, submitted *AAS journals*, arXiv:1801.05806
- Einstein, A. 1936, *Science*, 84, 506
- Gould, A. 1994, *ApJ*, 421, L75
- Gould, A. & Horne, K. 2013, *ApJ*, 779, L28
- Gould, A. & Loeb, A. 1992, *ApJ*, 396, 104
- Gould, A., Carey, S., & Yee, J. 2013, 2013spitz.prop.10036
- Gould, A., Carey, S., & Yee, J. 2014, 2014spitz.prop.11006

- Gould, A., Yee, J., & Carey, S., 2015a, 2015spitz.prop.12013
- Gould, A., Yee, J., & Carey, S., 2015b, 2015spitz.prop.12015
- Gould, A., Yee, J., & Carey, S., 2016, 2015spitz.prop.13005
- Gould, A., Yee, J., Carey, S., & Shvartzvald, Y. 2016, 2017spitz.prop.14012
- Gould, A., Dong, S., Gaudi, B.S. et al. 2010, ApJ, 720, 1073
- Griest, K. & Safizadeh, N. 1998, ApJ, 500, 37
- Han, C. & Gould, A. 1995, ApJ, 447, 53
- Han, C., Udalski, A., Gould, A. 2017a, AJ, 154, 133
- Han, C., Udalski, A., Gould, A. 2017b, AJ, 154, 223
- Hwang, K.-H., Kim, H.-W., Kim, D.-J., et al. 2018, JKAS, submitted, arXiv:1802.10246
- Kim, S.-L., Lee, C.-U., Park, B.-G., et al. 2016, JKAS, 49, 37
- Kim, D.-J., Kim, H.-W., Hwang, K.-H., et al., 2018a, AJ, 155, 76
- Kim, H.-W., Hwang, K.-H., Kim, D.-J., et al., 2018b, AJ, 155, 186
- Kim, H.-W., Hwang, K.-H., Kim, D.-J., et al., 2018c, AAS submitted, arXiv:1804.03352
- Mróz, P., Han, C., Udalski, A. et al. 2017, AJ, 153, 143
- Refsdal, S. 1966, MNRAS, 134, 315
- Rhie, S.H., Becker, A.C., Bennett, D.P., et al., 1999, ApJ, 522, 1037
- Ryu, Y.H., Yee, J.C., Udalski, A. et al. 2018a, AJ, 155, 4
- Ryu, Y.-H., et al. 2018b, in prep
- Schlaafy, E.F., Green, G.M., Lang, D. et al. 2018, ApJS, 234, 39
- Shvartzvald, Y., Yee, J.C., Calchi Novati, S. et al. 2017, ApJ, 840, L3
- Udalski, A. 2003, Acta Astron., 53, 291
- Udalski, A., Szymanski, M., Kaluzny, J., et al. 1994, Acta Astron., 44, 227
- Udalski, A., Jaroszyński, M., Paczyński, B, et al. 2005, ApJ, 628, L109.

- Udalski, A., Yee, J.C., Gould, A., et al. 2015, *ApJ*, 799, 237
- Udalski, A., Szymański, M.K., & Szymański, G. 2015, *Acta Astron.*, 65, 1.
- Woźniak, P. R. 2000, *Acta Astron.*, 50, 421
- Yee, J.C., Gould, A., Beichman, C., 2015, *ApJ*, 810, 155
- Zang, W., Hwang, K.-H., Kim, H.-W., et al. 2018, in prep

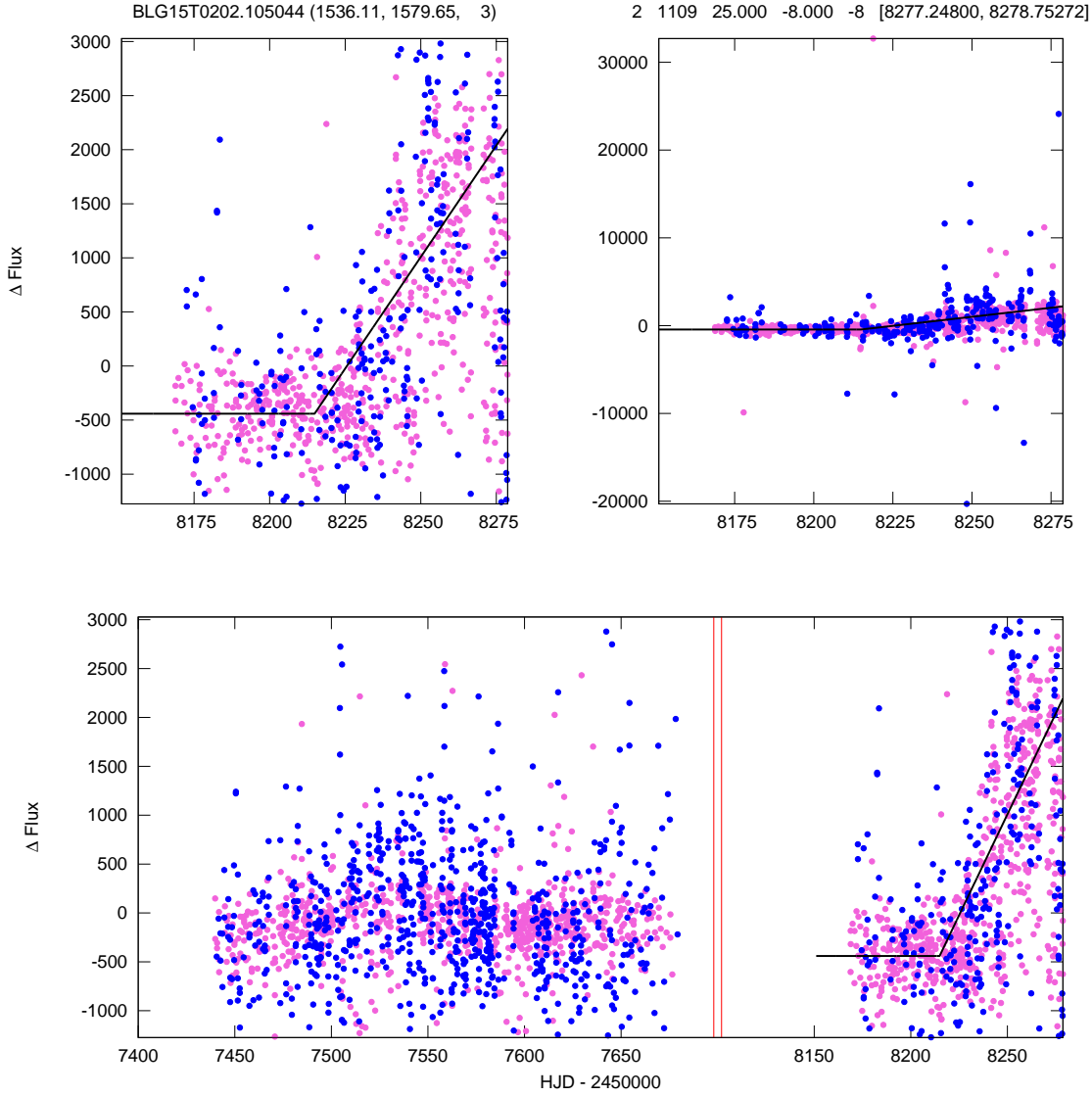


Fig. 1.— Four-panel display of a machine-selected candidate that was rejected by the operator as an “artifact”. The upper-left panel shows a model fit to the recent data. The KMTC data contributed the most to $\Delta\chi^2$, so the candidate name begins “BLG” (rather than “SAO” or “SSO”). The upper-right panel shows the same time frame but is extended vertically to include all data. The lower-right panel shows the same vertical range as the upper-left panel, but for the whole season. The lower-left panel shows 2016 data with different observatories aligned according to the 2018 model. Because KMTC contributes the most to $\Delta\chi^2$, it is shown in magenta. KMTS is shown in blue. KMTA is not shown because it did not contribute positively to $\Delta\chi^2$. The operator judged this to be an “artifact” mainly because the high-noise level is typical of artifacts generated by bleeds from a bright star contaminating faint stars further down the same column. The catalog star’s magnitude $I = 25.000$ indicates that it was too faint in the underlying DECam catalog (Schlafly et al. 2018) to make a proper estimate of its true I -band magnitude, making it a very plausible “host” for such artifacts. The lower-left panel did not, in this case, contribute to the “artifact” designation.

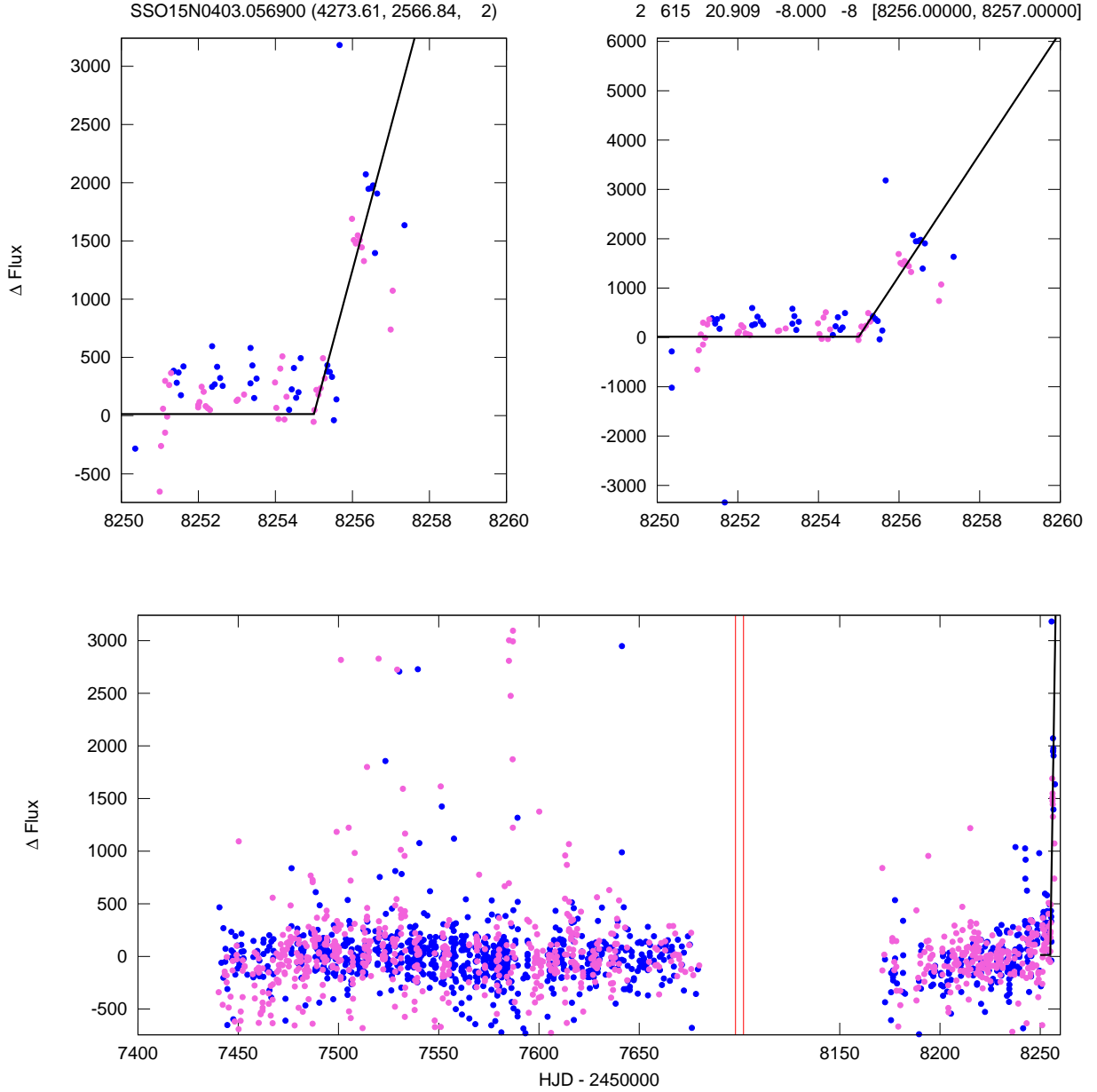


Fig. 2.— Four-panel display of machine-selected candidate that was accepted by the operator as “KMT-2018-BLG-0061”. The panel display is similar to Figure 1. The KMTS data contributed the most to $\Delta\chi^2$, so the candidate name begins “SSO” (rather than “BLG” or “SAO”). Because the alert-finder algorithm was first run on field BLG15 on 5 June 2018 (HJD 2458274), the actual selection took place 17 days after what is shown here. This can be seen on the alert website. This figure shows the result of running the alert-finder many times, each time incrementing t_{now} by one day and setting $t_{\text{last}} = t_{\text{now}} - 1$, in order to simulate its regular operation. This binary event was then first selected on HJD 2458257. In fact, at this point, although the light curve looks like “probable” microlensing, it is far from obvious that this is a binary microlens. When it was actually selected 17 days later, this binarity was clear. The fit on that later date did not at all match the binary’s features, but $\Delta\chi^2$ was roughly two times higher than shown here. See KMT alert website.

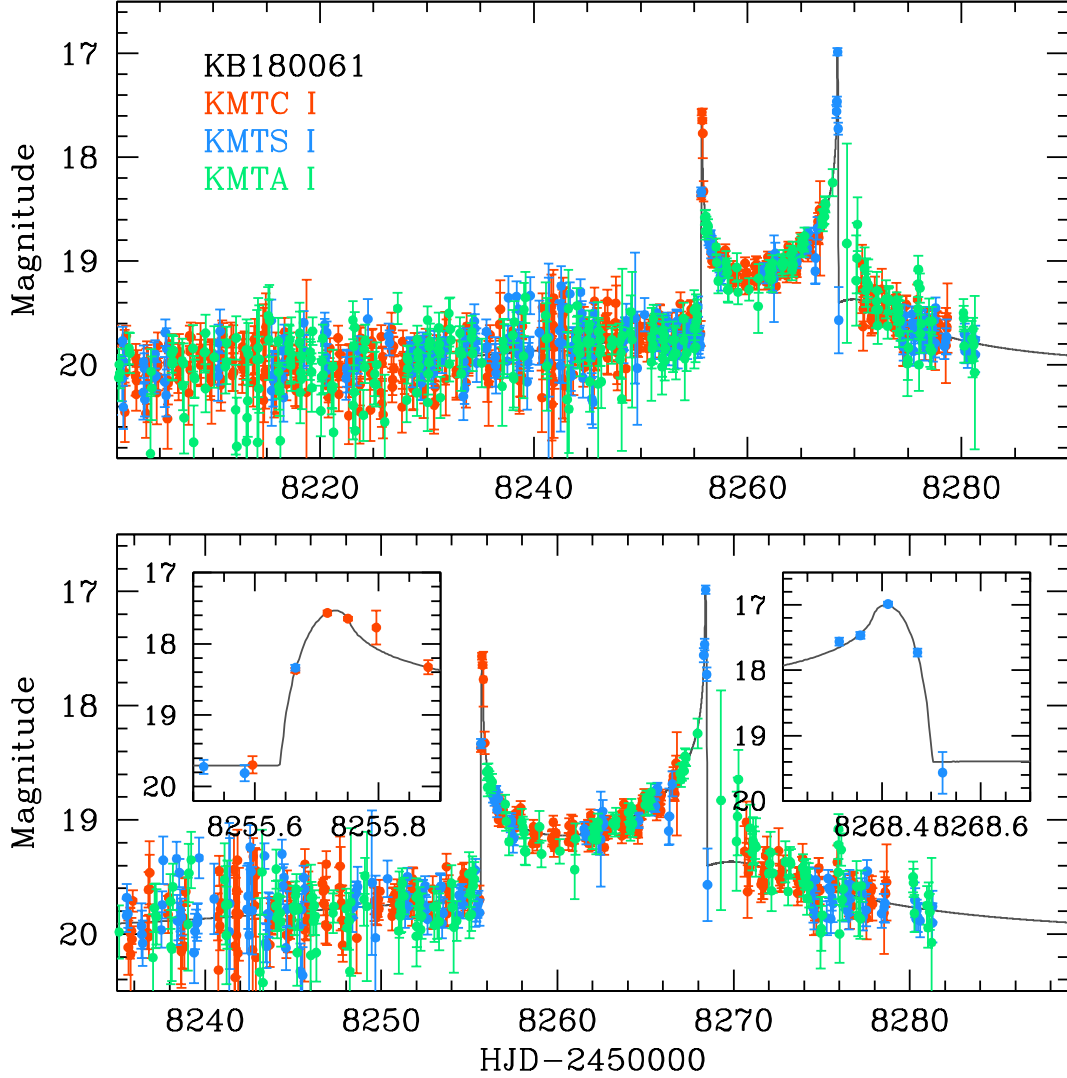


Fig. 3.— Subsequent development of KMT-2018-BLG-0061, whose four-panel display is shown in Figure 2. Tender loving care (TLC) pySIS reductions are shown, which are substantially better than the automated pySIS-pipeline reductions shown on the KMT alert website. By comparing this Figure with Figure 2, one can see that the alert was triggered by data in the trough, and that the much more dramatic KMTC data on the caustic entrance were actually “suppressed” by the algorithm because they were “outweighed” by the KMTS and KMTA data in the trough. Nevertheless, the event had $\Delta\chi^2 = 615$, easily exceeding the threshold of $\Delta\chi^2_{\text{thresh}} = 400$.